Journal of Nuclear Materials 401 (2010) 25–37

Contents lists available at ScienceDirect

Journal of Nuclear Materials

journal homepage: www.elsevier.com/locate/jnucmat

Anisotropic thermal creep of internally pressurized Zr–2.5Nb tubes

W. Li *, R.A. Holt

Department of Mechanical and Materials Engineering, Queen's University at Kingston, Ont., Canada K7L 3N6

ARTICLE INFO

Article history:
Received 26 November 2009
Accepted 18 March 2010

ABSTRACT

The anisotropy of creep of internally pressurized cold-worked Zr–2.5Nb tubes with different crystallographic textures is reported. The stress exponent n was determined to be about three at transverse stresses from 100 to 250 MPa with an activation energy of ~99.54 kJ/mol in the temperature range 300–400 °C. The stress exponent increased to ~6 for transverse stresses from 250 to 325 MPa. From this data an experimental regime of 350 °C and 300 MPa was established in which dislocation glide is the likely strain-producing mechanism. Creep tests were carried out under these conditions on internally pressurized Zr–2.5Nb tubes with 18 different textures. Creep strain and creep anisotropy (ratio of axial to transverse steady-state creep rate, $\dot{\varepsilon}_A/\dot{\varepsilon}_T$) exhibited strong dependence on crystallographic textures of the Zr–2.5Nb tubes. It was found that the values of ($\dot{\varepsilon}_A/\dot{\varepsilon}_T$) increased as the difference between the resolved faction of basal plane normals in the transverse and radial directions ($f_T - f_R$) increases. The tubes with the strongest radial texture showed a negative axial creep strain and a negative creep rate ratio ($\dot{\varepsilon}_A/\dot{\varepsilon}_T$) and tubes with a strong transverse texture exhibited the positive values of steady-state creep rate ratio ($\dot{\varepsilon}_A/\dot{\varepsilon}_T$) and good creep resistance in the transverse direction. These behaviors are *qualitatively* similar to those observed during irradiation creep, and also to the predictions of polycrystalline models for creep in which glide is the strain-producing mechanism and prismatic slip is the dominant system. A detailed analysis of the results using polycrystalline models may assist in understanding the anisotropy of irradiation creep.

1. Introduction

Zr–2.5Nb is used as pressure tube material in CANDU®[1] (CANada Deuterium Uranium) reactors, the Canadian-designed power reactors of PHWR type (Pressurized Heavy Water Reactor). CANDU reactors use heavy water (deuterium oxide) as a moderator and coolant, and natural uranium for fuel [1]. Zr–2.5Nb pressure tubes are manufactured by hot extrusion and are used in a cold-worked and stress-relieved condition. At the operating temperature (250–300 °C), Zr–2.5Nb consists predominantly of hexagonal close packed (hcp) α-Zr (containing about 0.6 wt.% Nb) with <10% body center cubic (bcc) β-Zr containing about 50 wt.% Nb, in which is embedded small amounts of Nb-depleted α and hcp ω phase [2]. The α-phase has a very strong crystallographic texture with basal plane (0 0 0 2) normals concentrated in the transverse direction of the tubes [2]. The mechanical properties of the tubes are largely dependent on microstructure and crystallographic texture of the α-phase [1].

With an internal pressure of about 10 MPa in a reactor core, the pressure tubes operate under a biaxial stress with a transverse stress of ~130 MPa and an axial stress of ~65 MPa [3]. During service, Zr–2.5Nb pressure tubes are irradiated by fast neutrons (2 and 4×10^{17} nm^{-2} s^{-1}, $E > 1$ MeV) at temperatures between ~250 and 310 °C [4]. The pressure tubes change in shape as a result of operating temperature, stress and fast neutron irradiation. The deformation is anisotropic because of the hcp crystal structure, combined with a strong crystallographic texture. These anisotropic dimensional changes occur as a result of irradiation growth, irradiation and thermal creep. Irradiation growth is the shape change due to irradiation damage at a constant volume under no external stress [5]. Irradiation and thermal creep cause a shape change at a constant volume under an applied stress with and without fast neutron irradiation [5]. Although thermal creep contributes only a small proportion (~10%) compared with irradiation creep (~70%) of the total deformation [6–8], it may contribute significantly to the anisotropic deformation of pressure tubes, especially at relatively high temperatures or stresses, for example, in the case of accident conditions. It also contributes significantly to the deformation at the outlet end of a fuel channel where fast neutron flux is relatively low, but temperature and bending moment are high [9].

Although creep may relax the stress concentration in the vicinity of a crack tip and mitigate the possibility of failure by the process of delayed hydride cracking [9,10], the anisotropic creep in pressure tubes generally limits their service life. Increases in diameter result in coolant bypassing the fuel and loss of cooling effectiveness, and may require de-rating of the reactor. The increase

* Corresponding author. Tel.: +1 613 533 3236; fax: +1 613 533 6610.
E-mail address: liwenjing@me.queensu.ca (W. Li).

[1] CANDU® is registered trademark of Atomic Energy of Canada Ltd. (AECL).

0022-3115/$ - see front matter © 2010 Elsevier B.V. All rights reserved.
doi:10.1016/j.jnucmat.2010.03.015

in length may exceed the allowances in the end hardware, requiring expensive maintenance, or even replacement of the tubes. The anisotropic dimensional changes and wall-thickness reduction increase the transverse stress accelerating the creep of the tubes. Therefore, there is a strong incentive to understand anisotropic creep and its relationship to crystallographic textures.

In a previous study of in-reactor deformation, Zr–2.5Nb tubes were only available with a few different crystallographic textures in which basal plane normals are concentrated in the transverse or radial direction [11,12]. This significantly restricts the understanding of the relationship between crystallographic texture and anisotropic creep. The strain-producing mechanism of irradiation creep of Zr alloy is thought to be dislocation glide, but polycrystalline models that predict the effect of texture on the anisotropy have been unable to rationalize the extreme behaviors of predominantly radial and predominantly transverse textures with realistic assumptions about the contributions of the different slip systems to the anisotropy of creep. In this paper, thermal creep of pressurized Zr–2.5Nb tubes with various textures will be reported for 18 different textures in a stress and temperature regime where dislocation glide is thought to be the dominant strain-producing mechanism. This provides an experimental database of anisotropic thermal creep response that can be used to develop and modify anisotropy models, and optimize crystallographic texture of Zr–2.5Nb tubes to improve creep resistance.

2. Materials

Zr–2.5Nb micro pressure tubes (MPTs) [13] and Zr–2.5Nb fuel sheathing (FS) tubes were used as experimental materials. Ingot chemical compositions of the tubes are given in Table 1. As shown in Table 1, Niobium (Nb) is the main alloying element. It has a low diffusion rate and its solubility limit is high, which can effectively enhance the creep strength of Zr–2.5Nb [14]. Oxygen and iron are two primary impurities. Oxygen can be introduced into the material during tube manufacturing procedure. It usually aggregates in α-phase and a high oxygen content can increase the hardness of the material [15]. Moreover, oxygen is reported to contribute to a strain aging phenomenon in the temperature range of 200–500 °C [5]. It was reported that Fe was largely associated with the β-phase and α–α sub-grain boundaries based on an analytical electron microscopic investigation [16,17]. Fe has a marked influence on apparent values for the self-diffusion coefficients in nominally pure α-zirconium [18,19].

The MPTs have a wall thickness of approximately 3 mm and an inner diameter of ~8 mm. They were made by a process developed at Nu-Tech Precision Metal Inc. to provide a similar microstructure and texture to standard CANDU pressure tubes (extruded at 815 °C with a ratio of 10:1, then 27% nominal cold-worked and finally stress relieved for 24 h at 400 °C, having a wall thickness of ~4.2 mm and an inner diameter of 103.5 mm) [13]. However, in order to obtain a range of different textures, the MPTs were extruded by varied combinations of temperatures and extrusion ratios[2] as given in Table 2. The different billet preparation, β-quenched (solution treated in β-phase field followed by quenching to room temperature) or slow cooled (solution treated in β-phase field followed by slow cooling to room temperature), provided a finer or coarser billet grain structure [13].

Zr–2.5Nb FS tubes used in the current project were manufactured for the experimental fuel in the AECL's WR1 reactor (which is now shut down) at Whiteshell Laboratories. The manufacturing route is given in Table 3. The finished tubes have an outer diameter of 10 mm and a wall thickness of 0.47 mm. The FS tubes provide a predominantly radial texture [12], i.e., most of basal plane normals is concentrated near the radial direction.

Table 1
Ingot chemical compositions of Zr–2.5Nb tubes.

Tubes	wt.%		Main impurities, ppm in weight		
	Zr + impurities	Nb	O	Fe	C
MPT62, 65, 63, 66	Balance	2.7	1160–1220	502–575	62–78
MPT72–79, 81, 82	Balance	2.7	1320–1360	1040–1110	76–80
FS	Balance	2.6–2.7	1030–1100	790–980	170–240

Table 2
MPTs extrusion temperatures and ratios.

Tubes no.	Extrusion		Billet preparation
	Temperature (°C)	Ratio	
MPT63	815	10:1	β-Quenched
MPT66	815	10:1	Slow cooled
MPT72, 73, 74	650	10:1	Slow cooled
MPT62	650	4:1	β-Quenched
MPT65, 76, 77, 79	650	4:1	Slow cooled
MPT81, 82	975	10:1	Slow cooled

Table 3
The general manufacturing route of Zr–2.5Nb fuel sheathing tubes [12].

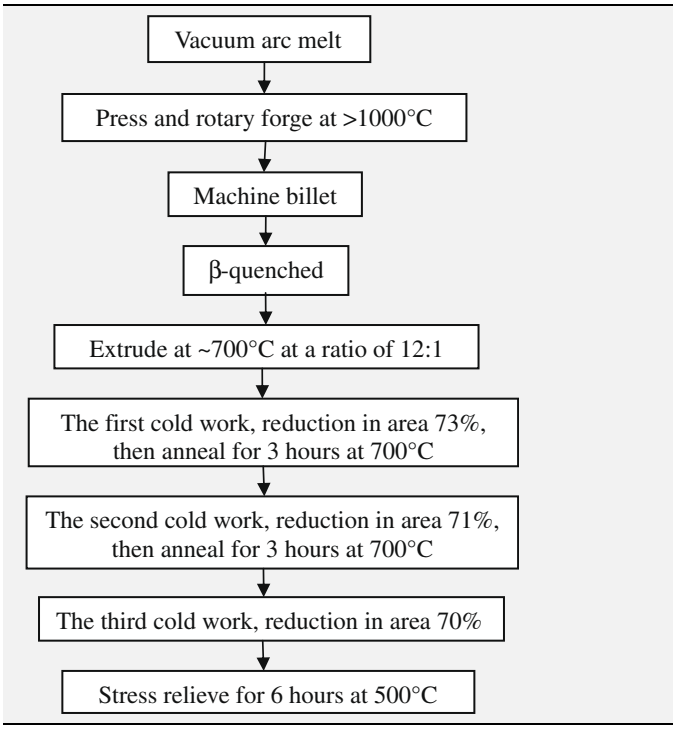

3. Experimental procedures

Textures of MPT and FS tubes were measured by neutron diffraction. The measurements were carried out on the E3 spectrometer at the National Research Universal (NRU) reactor in Chalk River Laboratories. For MPTs, the textures from the front ends, F

[2] The extrusion ratio is the ratio of the cross-sectional area of the tube before extrusion to the cross section area of the tube after extrusion.

(the ends emerging from extrusion press first), and the back ends, B (the ends emerging from extrusion press last), were measured. In order to obtain adequate diffracted intensity, a MPT was first cut into radial slices with a thickness of 0.5 mm and a length of 7 mm by an Isomet 1000 precision saw. Then these slices were glued or wrapped together by an aluminum foil with a consistent orientation to produce a bulk specimen approximately $6 \times 6 \times 7$ mm^3, as shown in Fig. 1. Sample preparation for FS tubes is similar to that of MPTs. However, due to the small wall thickness (0.47 mm), more pieces were cut to make a large enough sample.

Microstructures of MPTs in radial–transverse (normal to the axial direction of a tube) and radial–axial (normal to the transverse direction of a tube) sections were observed using a Philips TEM CM20 at 200 kV. To prepare the TEM samples, the tubes were first mechanically polished to a thickness of 0.1–0.15 mm and punched to obtain a 3 mm diameter disk. Then they were electrolytically thinned by a Tenupol-3 twin-jet electron polisher with an electrolyte of 5% perchloric acid and 95% methanol at temperature of −40 °C and 20 V. For FS tubes, the grain structure in axial–transverse section (normal to the radial direction) was observed because of the small wall thickness. For most of the MPT tubes, the microstructures only from the front ends were observed because the creep tests were performed on the specimens from the front ends, except for tubes MPT81 and 82, which were observed in both front and back ends.

Tubes with a wall thickness of ~0.46 mm and an outer diameter of ~10 mm (similar to the dimensions of FS tubes) were machined from the MPTs. Creep capsules were made by cutting the tube with a 40 mm length and electron beam welding Zr–2.5Nb end caps at each end, Fig. 2. After machining and welding, creep capsules were stress relieved for 24 h at 400 °C. The capsules were placed in a small vessel and pressurized with helium to give a specified pressure at the intended test temperature according to the ideal gas law, i.e., $P_1/T_1 = P_2/T_2$, where P_1 is the pressure at room temperature T_1, and P_2 is the pressure at the test temperature T_2. A small hole in one of end cap was then sealed by laser beam welding through a quartz window, leaving the capsule pressurized when the vessel was vented. Average through-wall transverse and axial stresses of each capsule at the test temperature were calculated according $\sigma_T = Pd/2t$ and $\sigma_A = Pd^2/(D^2 - d^2)$ [20], where P is the internal pressure, D and d are the outer and inner diameters, t is the wall thickness, and the subscripts T and A designate the transverse and the axial directions, respectively. The ratio of axial to transverse stress, R, is 0.48, which is close to the average stress state of a standard pressure tube in a CANDU reactor ($R \sim 0.49$). The specimen dimensions at room temperature (22 °C) were used to calculate the stresses because the effect of thermal expansion at testing temperature (300–400 °C) on dimensions is negligible (~0.2%) and has no effect on the calculated stress because all dimensions change by approximately the same factor.

Each creep capsule was contained in a stainless steel sample holder and placed in a Lindberg tube furnace. A thermocouple inserted into the holder's wall was used to monitor and record test temperatures. The earlier creep tests were performed in an air atmosphere in order to simplify the experimental apparatus. However, it was found that the appearance of thick white oxide on the machined end cap surface caused a significantly apparent strain in the axial direction despite a negligible effect on transverse (circumferential) strain (<0.01%). Therefore, for the results obtained from the tests in air, only the transverse strains are reported. In later tests, argon protection was used to eliminate any significant effect of oxidation. After each heating cycle, creep capsules were cooled in furnace for the first 30 min, and then in air to room temperature.

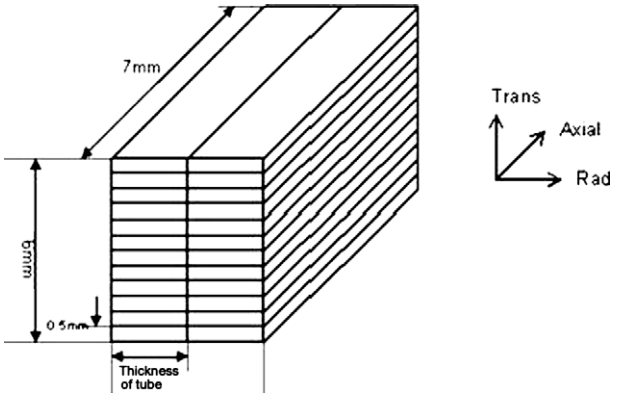

Fig. 1. Schematic diagram of a sample prepared from MPT for texture measurements.

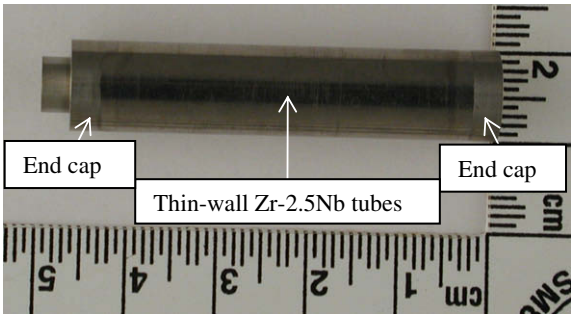

Fig. 2. Zr–2.5Nb creep capsule.

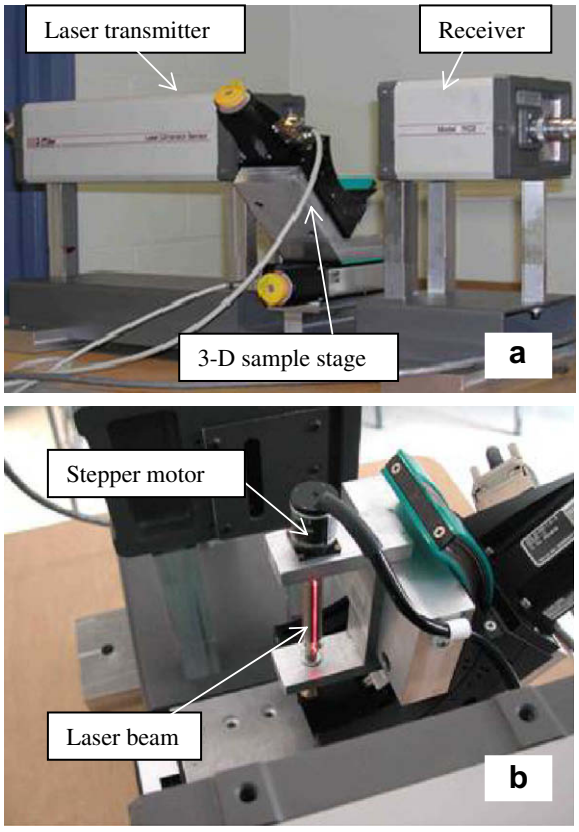

Fig. 3. (a) Z-Mike 1102 laser dimension sensor with a 3-D sample stage, (b) the sample stage at a vertical position for length measurements.

Changes in diameter and length (note that the length of the end caps was subtracted from the total measured length of creep capsules) were measured at room temperature by a laser dimensioning system, Fig. 3a. During the measurement, the specimen was set in a vertical or horizontal position at a sample stage, Fig. 3b, which was controlled by a SMC-Corvus high resolution position controller. For the length measurement, the capsule was set in a vertical position and rotated every 5° for 360° by a stepper motor as shown in Fig. 3b. For the diameter measurement, the specimen was set into the horizontal position. The diameter was measured at five axial locations and at each location the capsule was rotated at a 5° increment. The variation of transverse strains in five positions along the length is small, e.g., typically about 0.03% in the add-up transverse strain for a specimen heated at 350 °C under a transverse stress of 300 MPa. The entire measurement and specimen manipulation procedure was fully automated to minimize handling of the pressurized capsules. The values of length and diameter after each creep period were obtained by averaging the measurements in the vertical and horizontal positions, respectively. To assure an accurate measurement, a reference capsule was measured before and after each experimental specimen measurement. The repeatability of two reference measurements was within ±0.004 mm in length and ±0.001 mm in diameter. The accuracy of creep strains in both directions for an experimental capsule is thus approximately ±0.020%.

4. Results and analysis

4.1. Texture of Zr–2.5Nb tubes

Five general types of crystallographic textures were observed from the Zr–2.5Nb tubes after different manufacturing procedures. Firstly, a strong transverse texture were obtained in tubes MPT63 and 66, Fig. 4a, which were extruded at a temperature of 815 °C in the $\alpha + \beta$ phase and with an extrusion ratio of 10:1 to simulate actual pressure tube production. Secondly, a transverse/radial component of texture was observed in tubes MPT72, 73 and 74, which were extruded at 650 °C (a lower temperature in the $\alpha + \beta$ phase) with a ratio of 10:1. In these tubes, the basal plane normals from both ends are also mostly distributed in the transverse–radial plane and concentrated in the transverse direction, but, in general, they are more biased to the radial direction compared with tubes MPT66 and 63, as shown in Fig. 4b. Thirdly, tubes MPT62, 65, 76, 77 and 79 (extruded at 650 °C with a ratio of 4:1) showed a radial/transverse component of texture, in which the basal plane normals in both the front and back ends are distributed evenly in

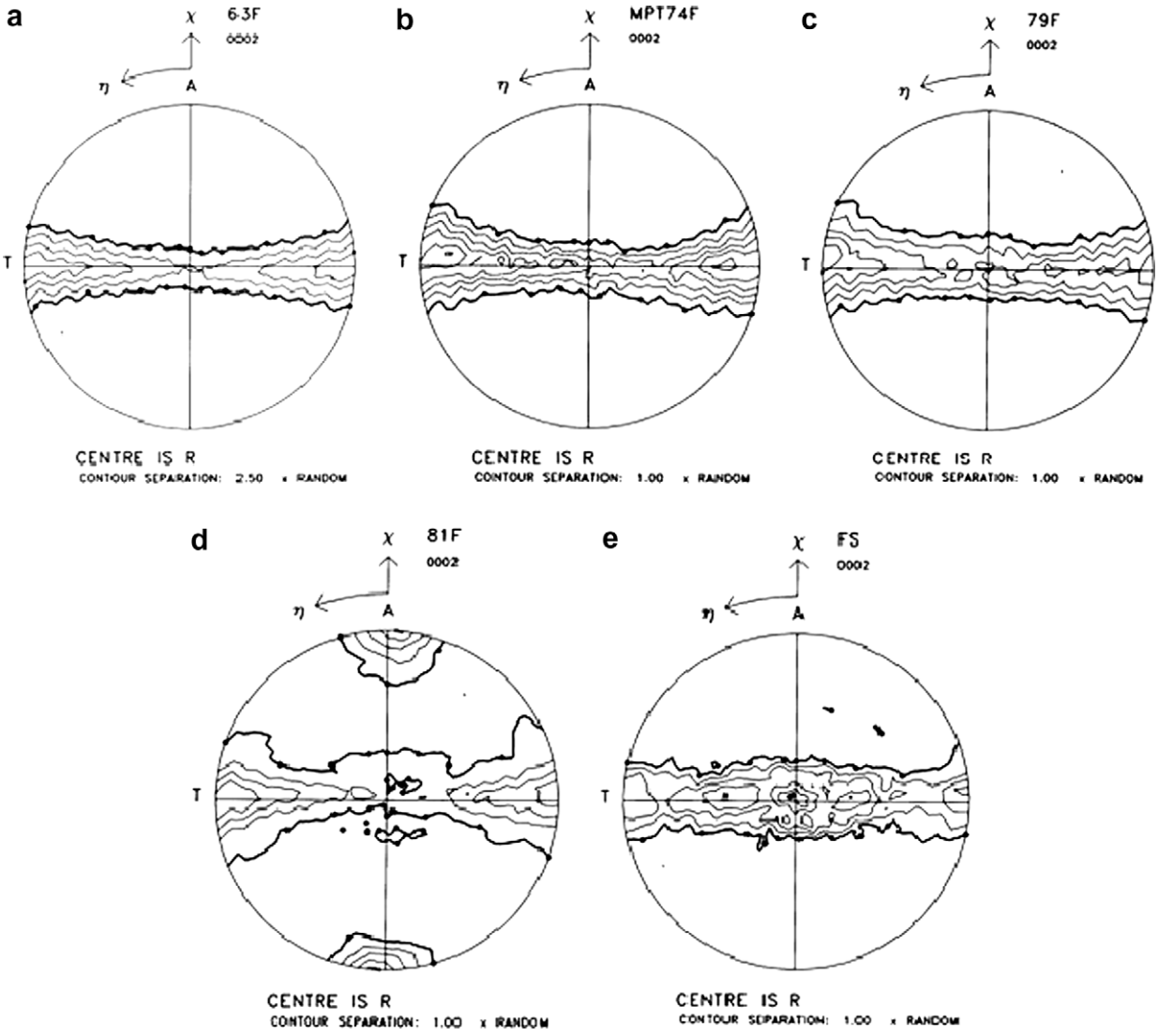

Fig. 4. Measured (0 0 0 2) pole figures of Zr–2.5Nb tubes.

the radial–transverse plane, see Fig. 4c. Fourthly, tubes MPT81 and 82 (extruded at 975 °C with a ratio of 10:1) have a significant component of basal plane normals in the axial direction, especially from the tubes in the front end, Fig. 4d. For the back ends of tubes MPT81 and 82, the textures are very similar to those of tubes MPT63 and 66. In general the textures of the MPT's are consistent with the current understanding of the development of texture in Zr–2.5Nb during extrusion [13,21–23]. Cold drawing has little effect on the texture developed during extrusion [13,21–23] aside from a reduction in the axial component in tubes MPT81 and 82.

The FS tubes provide the strongest radial texture, in which most of the basal plane normals are concentrated near the radial direction with maxima ±30° away from the radial direction in the radial–transverse plane, Fig. 4e. This is typical of zirconium alloy fuel sheathing [24].

The resolved factors of basal plane normals, f_A, f_T and f_R in the axial, transverse and radial directions of a tube, are used to numerically represent the distributions of (0 0 0 2) plane normals. It is a factor used to represent crystallographic texture of a material. They are calculated by [25]:

$$F_d = \sum_{i=1}^{j} V(\theta_i)\cos^2\theta_i$$

where the basal pole figure is divided into a grid of j elements and $V(\theta_i)$ is the volume fraction of the crystals with basal plane normals in an element of the pole figure grid at an angle θ_i to a reference direction; d designates the transverse (T), radial (R) or axial (A) direction.

Fig. 5 depicts the variation of the resolved factors of basal plane normals in three principal directions in order of f_T. It can be seen that the resolved factors f_T in the transverse direction vary from 0.389 to 0.582, and the values of f_R vary from 0.550 to 0.326, showing a variation from dominant radial to transverse textures. As seen in Fig. 5, in general, for the tubes extruded in the α + β-phase region, the values of f_T vary in a decreasing order from tubes MPT63, 66, MPT72, 73, 74 to MPT62, 65, 76, 77, 79; on the contrary, the values of f_R increase with decreasing values in f_T. The values of f_A seem to be insensitive to changes in the tubes and are the smallest, generally between 0.04 and 0.09. However, for the tubes extruded in the β-phase region, the f_A values for tubes MPT81 and 82 are higher and larger than 0.1, especially in the front ends of the tubes, i.e., f_A = 0.223 (MPT81F) and f_A = 0.181 (MPT82F). It is evident that FS tubes have the strongest radial texture ($f_T < f_R$) among the tubes. Clearly, the Zr–2.5Nb tubes provide a diverse range of textures with which to investigate the effect of texture on anisotropic creep in this pressure tube material.

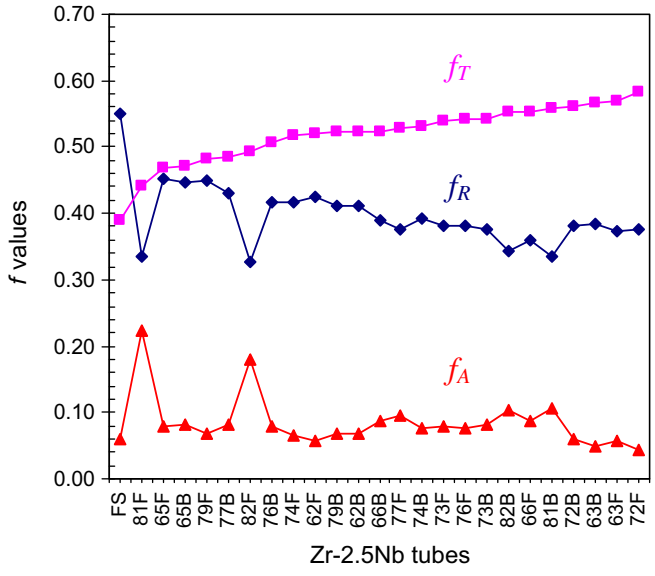

Fig. 5. Variation of resolved factors of basal plane normals for Zr–2.5Nb tubes.

4.2. Microstructures of Zr–2.5Nb tubes

For most of the Zr–2.5Nb MPTs, the microstructures comprise highly elongated α-grains and thin films of β-phase surrounding the α grains, see Fig. 6a, as is the case of CANDU pressure tubes. Grain structures of tubes MPT66F, 63F, 72F, 73F, 74F, 76F, 77F, 79F and 65F are of this type. However, some billet preparations and extrusion conditions affect grain sizes of these tubes. For example, tube MPT63 (extruded after a β-quenched billet) has a finer grain size with a thickness of ~0.2 μm in the α phase; while the tubes extruded after a slow-cooled billet have a larger grain thickness, i.e., tubes MPT72F, 73F, 74F, and 66F (extrusion ratio = 10:1) have a grain thickness in the α phase varying from 0.4 to 0.8 μm, and tubes MPT65F, 76F, 77F, and 79F (extrusion ratio = 4:1) have a thickness varying from 0.7 to 1.5 μm. A second type of α-grain structure (tubes MPT62F, 81B and 82B) appears equiaxed in the radial–transverse section with the β-phase distributed at grain boundaries and corners with a grain diameter of 0.2–0.5 μm, Fig. 6b. The third type of microstructure (the front ends of tubes MPT81 and 82) appears as Widmanstätten α-plates with continuous β-Zr surrounding the plates, Fig. 6c, and a thickness of less than 0.5 μm. Finally, the FS microstructure consists of flattened α-grains (light) with discontinuously distributed β-phase (dark), Fig. 6d. These microstructures are consistent with previous studies of the development of microstructure and texture during extrusion of Zr–2.5Nb [13,21–23].

4.3. Creep tests under different stresses and temperatures

A group of FS capsules were tested in air under a range of transverse stresses at 350 °C at nominal transverse stresses from 100 MPa to 300 MPa in increments of 50 MPa and at 400 °C at nominal transverse stresses of 100 MPa, 150 MPa and 200 MPa. Transverse creep strains as a function of creep time and transverse steady-state creep rates as a function of transverse stresses are depicted in Fig. 7. In analyzing the data, steady state was assumed to be reached when the curves of transverse creep strain versus creep time become approximately liner after a sharp decreasing of strain-rate during the primary creep stage. In most cases the creep tests were terminated at about 1% creep strain in the transverse direction to avoid the possibility of the specimens rupturing during handling. Steady-state creep rate was taken as the value of the slope by plotting a linear trend line from the last four data points in a given creep curve (usually about 0.5% strain). Note that the tests may not have reached a true steady state. Errors in these "steady-state" creep rates were estimated from the uncertainty of slope of the linear trend line and marked as error bars in Fig. 7b and d.

A general increase in creep with transverse stress at both 350 °C and 400 °C is clear, Fig. 7a–d. However, there is a complex or mixed creep behavior for the capsules under a transverse stress of 200 MPa and 250 MPa at 350 °C. As shown in Fig. 7a, at the first 100 h of heating, their transverse creep strains increase with similar steps, but after that period the creep capsule under a transverse stress of 250 MPa exhibited a smaller strain than the specimen under a transverse stress of 200 MPa until 400 h of heating. A sharp jump in the creep curve for the capsule under a transverse stress of 250 MPa occurred at the heating time of 400–580 h, and after that the curve becomes smooth until 1% transverse strain. This behavior may be associated with strain aging [5].

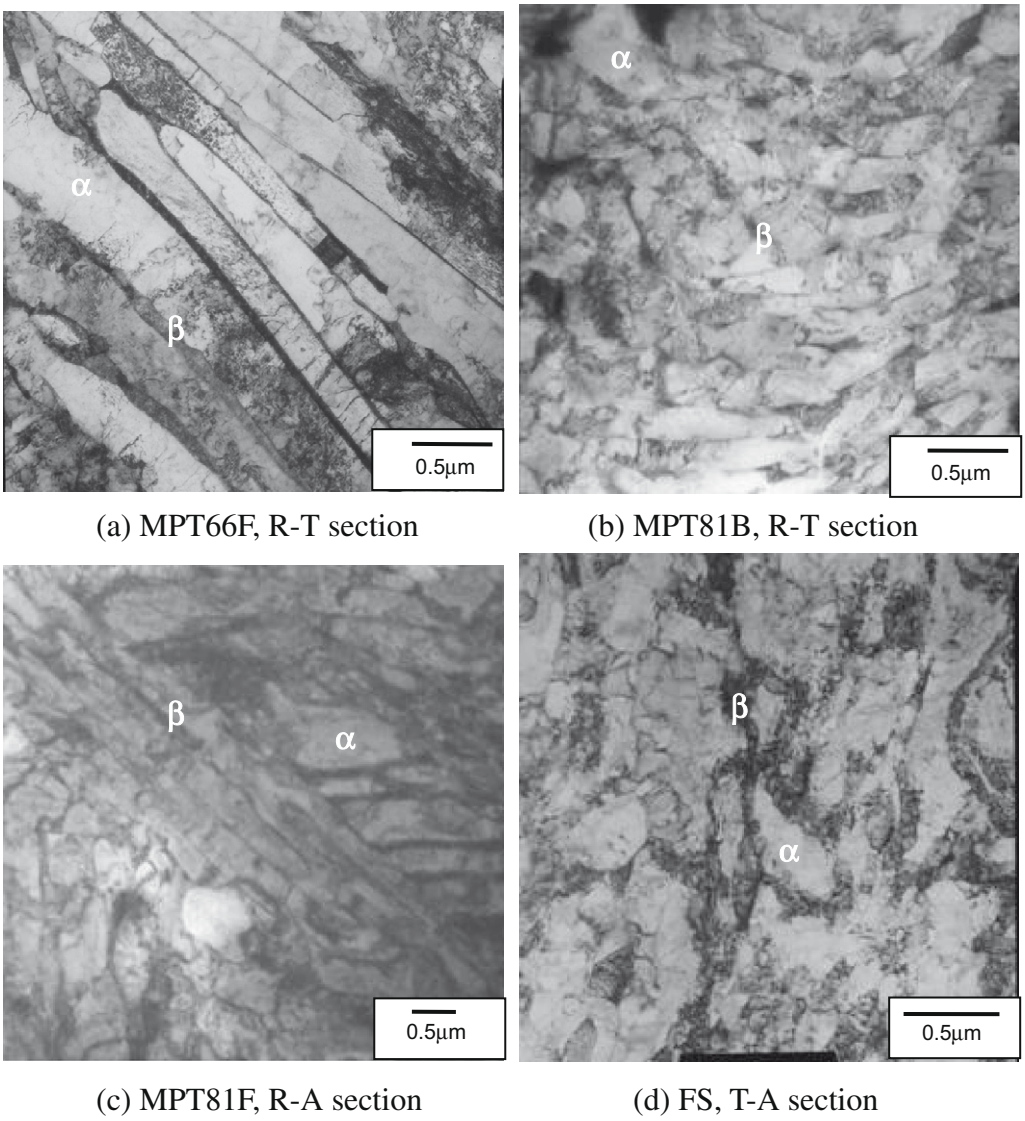

Fig. 6. TEM microstructures of Zr–2.5Nb MPT and FS tubes.

In the subsequent tests, because argon gas protection was introduced into the experimental set-up, both transverse and axial strains were measured. Creep tests were carried out on FS, MPT66 and MPT63 capsules under a nominal transverse stress of 275 MPa, 300 MPa and 325 MPa at 350 °C. Creep strains as a function of time are depicted in Fig. 8 and the steady-state creep rates are given in Table 4. It is evident that all tested capsules exhibit positive transverse strains and there is an increase in the transverse creep strains and rates with increasing transverse stress. However, the creep behavior in the axial direction is more complex, as seen in Fig. 8b, d and f. For example, the FS capsule under a nominal transverse stress of 275 MPa first exhibited a sharp increasing transient strain in the axial direction, and then the creep strain went to a decreasing trend (although the axial strain remains positive throughout), Fig. 8b. For the FS capsules under a transverse stress of 300 MPa and 325 MPa, the axial strains eventually became negative after a positive strain in the primary stage. For both MPT63 and MPT66 capsules, the axial strains are positive under all test conditions. However, the creep behavior in the axial direction for the MPT66 capsules also shows a complex profile, Fig. 8d. The capsule under a transverse stress of 275 MPa showed the highest axial strains in all three MPT66 capsules. The reason for this result is not clear. It could be related to stress relieving, recovery, or ongoing phase transformation in the β-phase. But in general, the creep strains and steady-state creep rates increase as expected with stress in both directions as shown in the figures and Table 4. Here, this complex transient behavior will not be considered and only the long term "steady-state" creep rates are discussed.

4.4. Creep of Zr–2.5Nb tubes with varied crystallographic textures and microstructures

Creep tests on the MPTs with different crystallographic textures were carried out under a nominal transverse stress of 300 MPa and a temperature of 350 °C. Fig. 9 shows creep strain in both transverse and axial directions versus time. Table 5 provides the values of steady-state creep rate for each capsule. In the figures, the capsules from tubes made at the same nominal extrusion conditions are plotted in the same color. Note that F or B in the parentheses denotes that the capsule was from the front or back end of the tube, and S or Q denotes that the billet of the tube was prepared by slow cooling or β-quench.

In the transverse direction, Fig. 9a, capsule FS23 crept fastest and took less than 100 h to reach 1% transverse strain with the

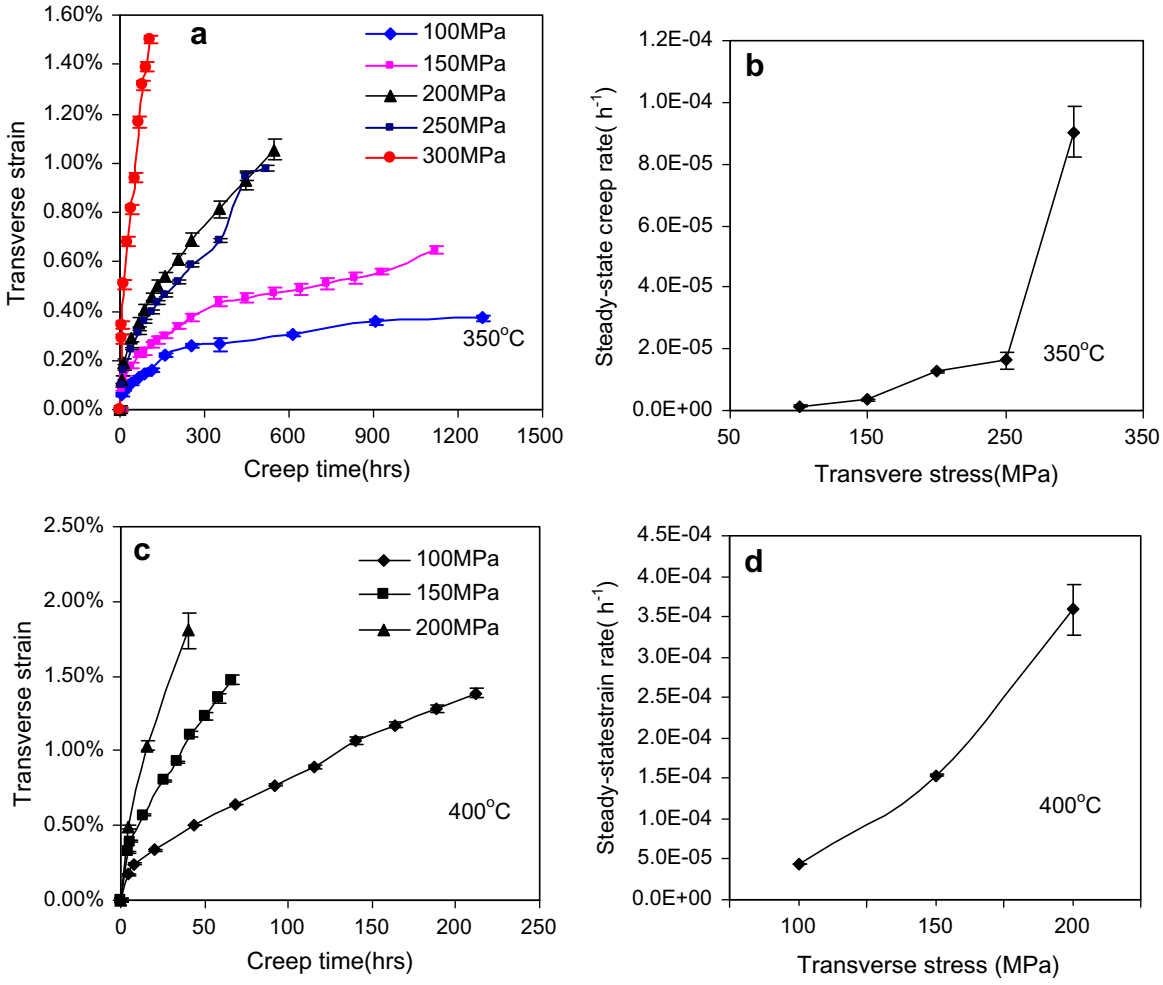

Fig. 7. Creep of internally pressurized FS capsules tested in air under different transverse stresses at 350 °C and 400 °C.

highest value of steady-state creep rate in Table 5. At the other extreme, capsules MPT82-01(F,S) and 66-05(F,S) took over 1200 h to reach approximately 1% transverse strain and MPT 81-02(F,S) took over 2200 h to reach about 0.7%. The transverse creep curves of capsules MPT72-02(F,S), 73-02(F,S), 74-01(F,S) (extrusion ratio of 10:1 at 650 °C, billet preparation by slow cool) and capsules MPT76-03(F,S), 76-04(F,S), 77-01(F,S), 79-02(F,S) and 65-01(F,S) (extrusion ratio of 4:1 at 650 °C, billet preparation by slow cool) exhibited intermediate creep strains. Capsules MPT72-02(F,S) and 73-02(F,S) had a similar creep behavior, reaching 1% strain in the transverse direction after ~800 h. MPT74-01(F,S) showed a faster creep behavior in the transverse direction which may correspond to the smaller f_T (0.518) value compared with those of MPT72F (f_T = 0.582) and MPT73F (f_T = 0.538) as shown in Fig. 5. Of the tubes made with an extrusion ratio of 4:1 at 650 °C, capsules MPT76-03(F,S), 76-04(F,S), and 77-01(F,S) exhibited a similar creep behavior; capsules MPT79-02(F,S) and 65-01(F,S) crept faster in the tubes possibly because they have a smaller component of basal plane normals in the transverse direction (f_T) in Fig. 5.

Specimens from tubes extruded from β-quenched billets, such as capsules MPT63-03(F,Q), 63-08(F,Q) (extrusion ratio of 10:1 at 815 °C) and 62-01(F,Q) (extrusion ratio of 4:1 at 650 °C), exhibited faster creep behaviors and higher steady-state creep rates than the specimens with slow-cooled billet preparation. Moreover, the specimens from the back ends of tubes MPT81 and 82, capsules MPT81-03(B,S), MPT82-03(B,S) and MPT82-05(B,S), crept much faster than the front-end specimens and the steady-state creep rates are approximately 5–9 times higher. These different creep behaviors between the front and back end capsules in tubes MPT81 and 82 may be related to the texture and microstructure variations along the axial direction of the tubes. This indicates that good control of the extrusion procedures and parameters is important to obtain a uniform creep behavior along the tubes.

In the axial direction, Fig. 9b, only specimen FS23 exhibited negative axial strain and a negative steady-state creep rate, Table 5, which correlate with its fast creep behavior in the transverse direction. Capsule MPT81-02(F,S) showed the slowest axial creep, Table 5, possibly because of a relatively strong axial component of basal plane normals, as shown in Fig. 5. After MPT81-02(F,S), capsules MPT65-01(F,S), 76-03(F,S), 76-04(F,S), 77-01(F,S), 79-02(F,S) and 82-01(F,S) showed lower axial creep rates, Table 5. The axial creep curve of MPT66-05(F,S) falls into the middle part of the overall plots in Fig. 9b. Capsules MPT72-02(F,S), 73-02(F,S) and 74-01(F,S) have the similar axial creep behavior because of the same nominal extrusion conditions and they crept faster than MPT66-05(F,S). As with the transverse creep behavior, capsules MPT81-03(B,S), 82-03(B,S), 82-05(B,S), 62-01(F,Q), 63-03(F,Q) and 63-08(F,Q) all shows the highest positive axial rates in Table 5.

It can be seen that the capsules from the tubes extruded at the same nominal conditions exhibit somewhat different creep behaviors. This variation may be related to the texture variation of the tubes in the same group, as is the slight discrepancy in the values of the resolved factors of basal plane normals in Fig. 5. The discrepancies in creep behavior may also be due to the texture gradient

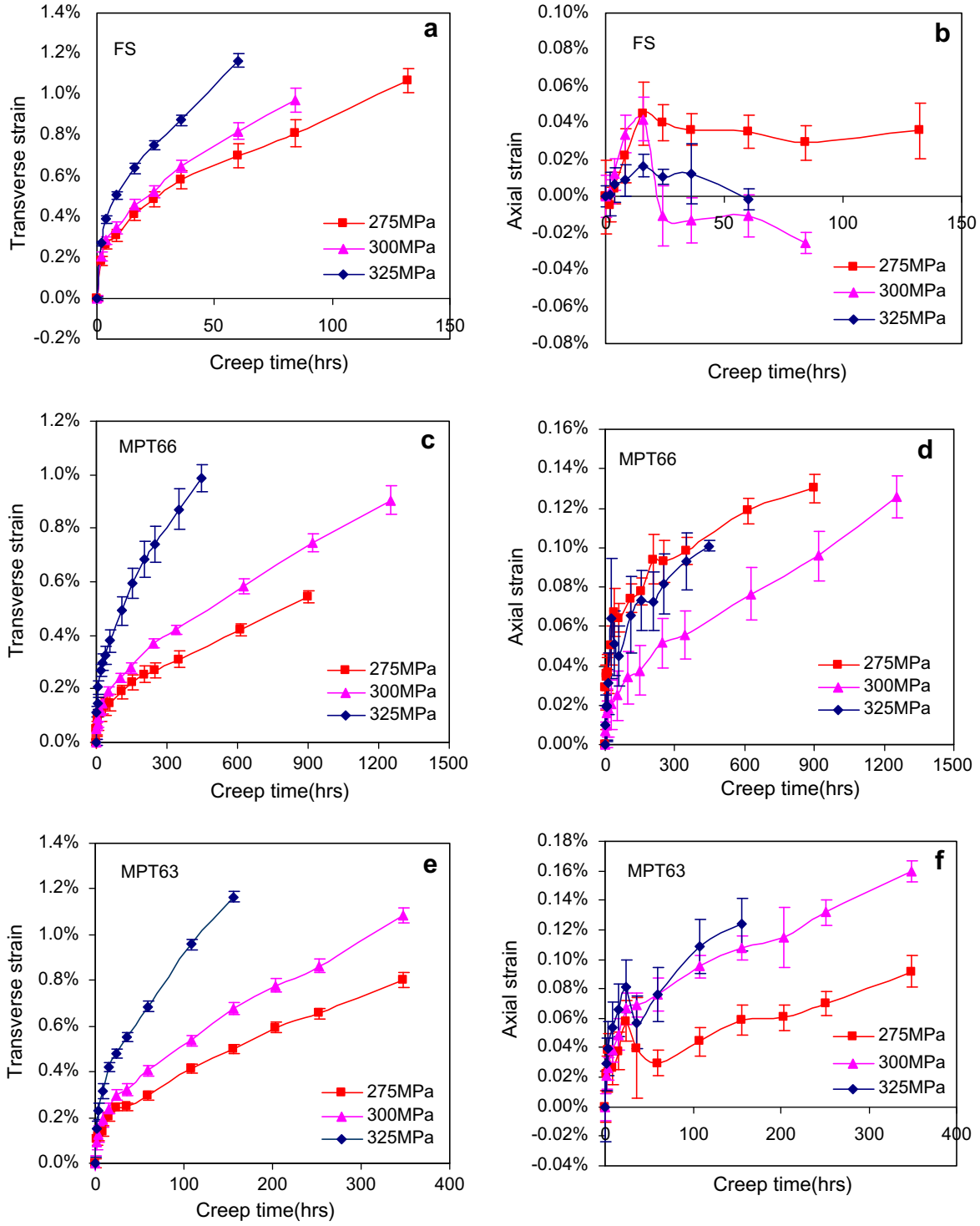

Fig. 8. Creep of internally pressurized FS, MPT66 and MPT63 capsules tested in argon under a nominal transverse stress of 275 MPa, 300 MPa and 325 MPa at 350 °C.

through the wall and along the axial direction of the tubes. Because the creep capsules were manufactured from a reduced section, the measured texture, representing a through-wall average, may not exactly represent the texture of the tested capsules. Li et al. [21] observed through-wall variations in micro pressure tubes after extrusion, although these were not statistically significant, except at the front end of those extruded after preheating in the β-phase. Judge [26] did not observe such variations in the extrusions from which MPT72-82 were made except at the front ends of tubes MPT81and 82. Capsule MPT66-05(F,S) (same nominal extrusion conditions as the pressure tubes in CANDU reactors) exhibited a good transverse creep resistance, it shows relatively high creep strains and steady-state creep rate in the axial direction. Capsule MPT81-02(F,S) showed the lowest creep rate in both the axial and transverse directions among all the tested capsules, indicating the best creep resistance in the tested tubes.

Table 4
Steady-state creep rates and ratios for internally pressurized FS, MPT66 and MPT63 capsules tested under different transverse stresses at 350 °C.

Tubes	Transverse stress (MPa)	Steady-state creep rate ($\times 10^{-5}$ h^{-1})		Steady-state creep rate ratio ($\dot{\varepsilon}_A/\dot{\varepsilon}_T$) ($\times 10^{-2}$)
		Axial	Transverse	
FS	275	−0.12 ± 0.02	5.08 ± 0.12	−2.34 ± 0.47
	300	−0.21 ± 0.11	7.28 ± 0.50	−2.86 ± 1.54
	325	−0.38 ± 0.10	11.84 ± 0.33	−3.24 ± 0.84
MPT66	275	0.06 ± 0.01	0.42 ± 0.00	14.03 ± 1.46
	300	0.08 ± 0.00	0.53 ± 0.02	14.21 ± 0.78
	325	0.12 ± 0.01	1.27 ± 0.03	9.06 ± 1.06
MPT63	275	0.18 ± 0.03	1.55 ± 0.07	11.59 ± 2.05
	300	0.28 ± 0.02	2.13 ± 0.07	13.15 ± 1.21
	325	0.56 ± 0.07	5.14 ± 0.23	10.88 ± 1.54

5. Discussion

5.1. Stress exponent n

The stress exponent, n, based on the equation, $\dot{\varepsilon} = B\sigma^n$ [5], can be determined from the tests by applying a range of stresses at a constant temperature, where B is a temperature dependent material parameter, $\dot{\varepsilon}$ is the steady-state creep rate and σ is the applied stress. Fig. 10a shows log $\dot{\varepsilon}$ versus log σ from the results of FS capsules tested under transverse stress ranging from 100 MPa to 325 MPa at 350 °C and from 100 MPa to 200 MPa at 400 °C. The slopes of the linear plot give the value of the stress exponent n. It can be seen that under a transverse stress below 250 MPa, n is about 2.88–3.02 for 350 °C and 400 °C. This value is typical expected for pure dislocation creep ($n = 3$) [27] in which the rate is controlled by climb and the strain-producing mechanism is glide.

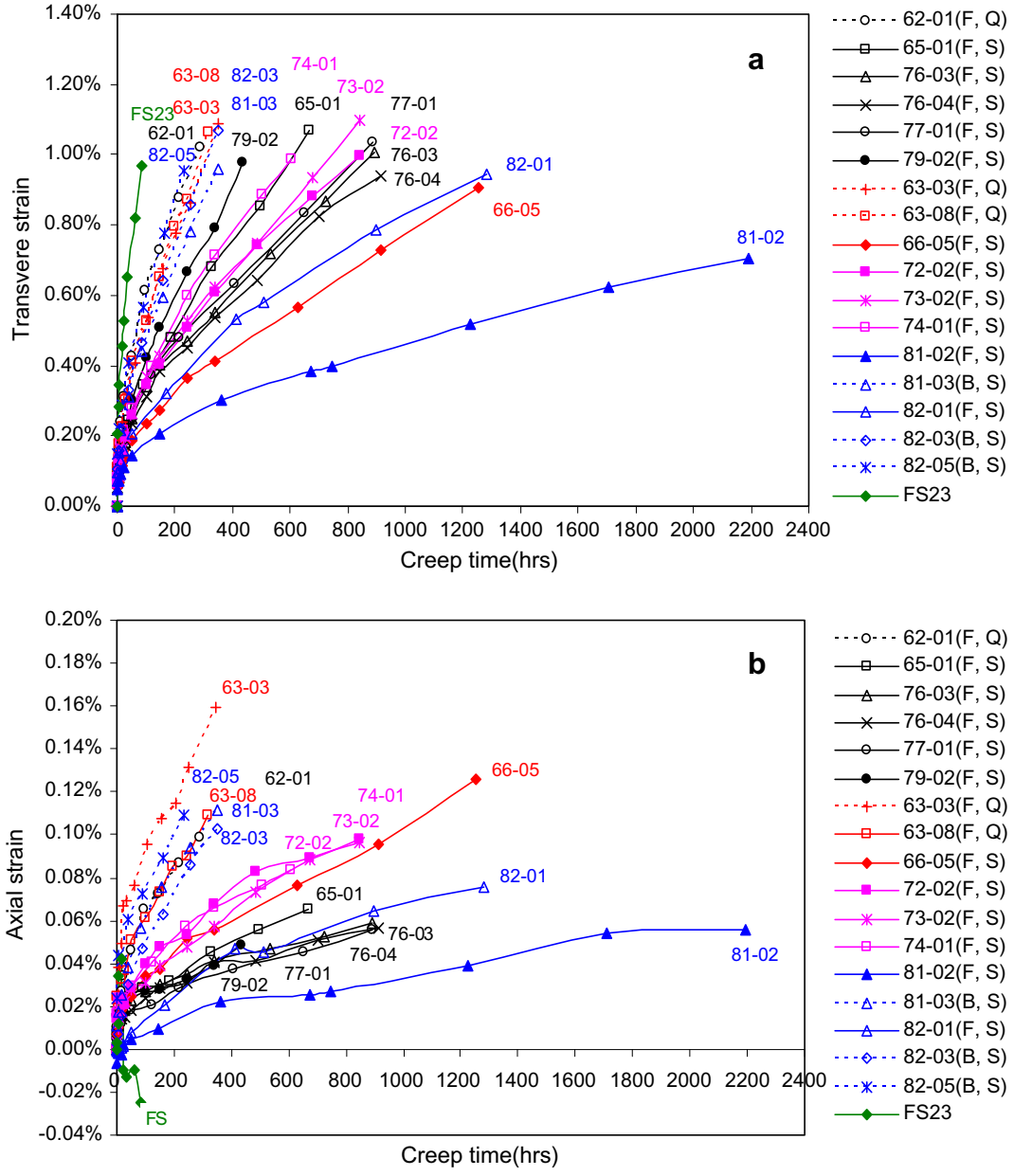

Fig. 9. Creep strains versus creep time for internally pressurized FS and MPT capsules with different textures under a nominal transverse stress of 300 MPa at 350 °C (a) in the transverse direction, (b) in the axial direction. Note that error bar on creep strains were not marked for a clear illustration.

Table 5
Steady-state creep rates and ratios for internally pressurized FS and MPT capsules tested under a nominal transverse stress of 300 MPa at 350 °C.

Sample no.	Steady-state creep rate ($\times 10^{-6}$ h^{-1})		Steady-state creep rate ratios ($\dot{\varepsilon}_A/\dot{\varepsilon}_T$) ($\times 10^{-2}$)
	Axial	Transverse	
MPT63-03(F,Q)	2.80 ± 0.24	21.30 ± 0.74	13.15 ± 1.21
MPT63-08(F,Q)	2.07 ± 0.20	23.81 ± 1.72	8.67 ± 1.06
MPT66-05(F,S)	0.76 ± 0.04	5.34 ± 0.16	14.21 ± 0.78
MPT72-02(F,S)	0.56 ± 0.10	7.58 ± 0.36	7.39 ± 1.33
MPT73-02(F,S)	0.78 ± 0.09	9.46 ± 0.12	8.23 ± 0.97
MPT74-01(F,S)	0.72 ± 0.05	10.60 ± 0.26	6.74 ± 0.47
MPT62-01(F,Q)	1.79 ± 0.06	20.90 ± 0.49	8.56 ± 0.36
MPT65-01(F,S)	0.68 ± 0.05	12.08 ± 0.45	5.64 ± 0.47
MPT76-03(F,S)	0.32 ± 0.01	8.22 ± 0.12	3.85 ± 0.19
MPT76-04(F,S)	0.30 ± 0.04	7.07 ± 0.43	4.26 ± 0.63
MPT77-01(F,S)	0.41 ± 0.02	8.28 ± 0.06	4.89 ± 0.20
MPT79-02(F,S)	0.71 ± 0.09	16.03 ± 0.87	4.45 ± 0.59
MPT81-02(F,S)	0.21 ± 0.04	2.13 ± 0.12	9.78 ± 2.12
MPT81-03(B,S)	2.05 ± 0.12	19.57 ± 0.46	10.45 ± 0.65
MPT82-01(F,S)	0.37 ± 0.04	4.81 ± 0.20	7.63 ± 0.97
MPT82-03(B,S)	2.15 ± 0.10	22.89 ± 0.44	9.38 ± 0.48
MPT82-05(B,S)	2.52 ± 0.06	28.45 ± 1.09	8.85 ± 0.40
FS23	−2.08 ± 1.11	72.80 ± 5.00	−2.86 ± 1.54

It is significantly higher than that expected for diffusional creep mechanisms (n = 1–2). The stress exponent increases to $\geqslant 7$ when the transverse stresses are in the range from 250 MPa to 325 MPa, which clearly indicates that dislocation glide is the strain-producing mechanism [28]. Fig. 10b and c shows the stress exponent n determined from both transverse and axial directions in FS, MPT66 and MPT63 capsules under a transverse stress of 275–325 MPa at 350 °C. For FS capsules, the plots in the transverse direction included the result under a transverse stress of 250 MPa as shown in Fig. 10b. It is shown that the n values vary in the range of 3.9–7.3 with an average value of 6.4, again consistent with dislocation creep [28].

The stress exponent derived from the experimental data varies with stress which may indicate that the deformation mechanism changes. However, over the whole stress range tested, the n value is substantially greater than one. Kohn [29] reported the values of the stress exponent increase from a minimum of 2 at low stresses (40–150 MPa) to 5.3 at a higher (150–200 MPa) in Zr–2.5Nb FS tubes based on the minimum out-of-reactor (thermal) creep rates versus stresses at a temperature of 350 °C. Nuttall [30] showed that for Zr–2.6Nb at 510 °C, the stress exponent also strongly depends on stresses, in particular, when the stress is higher than 200 MPa,

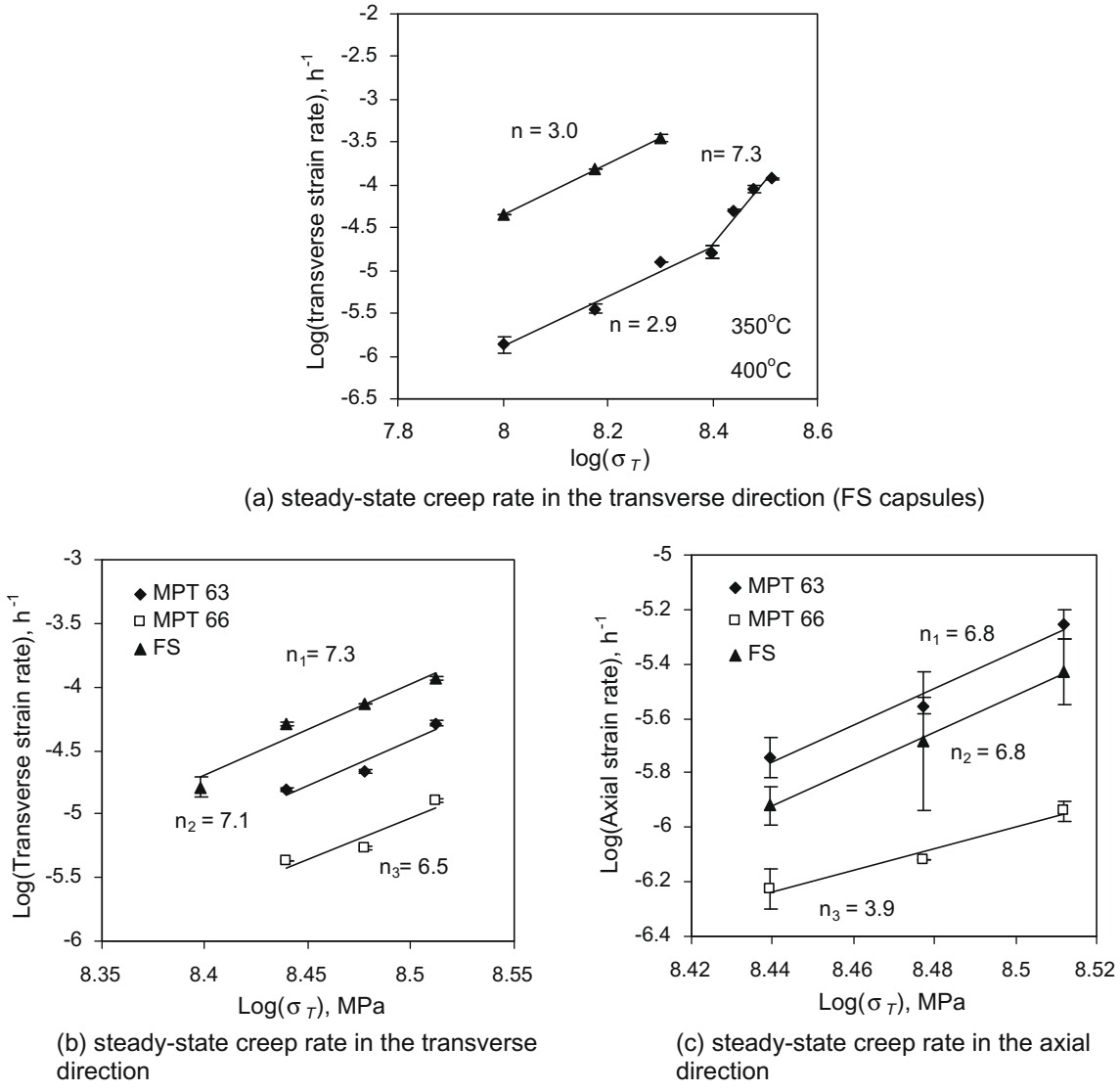

(a) steady-state creep rate in the transverse direction (FS capsules)

(b) steady-state creep rate in the transverse direction

(c) steady-state creep rate in the axial direction

Fig. 10. Stress exponent n obtained by log–log relationship of steady-state creep rate as a function of transverse stress.

the n value increases rapidly. Christodoulou et al. [31] stated that for the rates lower than 5×10^{-7} h^{-1}, all Zr alloys exhibit values of n lower than five. Hayes et al. [32] reviewed thermal creep of zirconium from various studies. They established a relationship between diffusion coefficient compensated steady-state creep rates and shear modulus compensated steady-state stress, which determined the value of stress exponent n to eliminate the differences in impurity contents and test conditions. At intermediate stresses ($\sigma/G = 1 \times 10^{-4}$–$1 \times 10^{-2}$, G is the shear modulus), a constant stress exponent value of 6.4 was obtained, indicating a power law creep mechanism, and it is consistent with the obtained average value from the tests under transverse stress from 250 MPa to 325 MPa.

Hence, the values of stress exponent indicate that dislocation creep is the likely operating mechanism of creep in the range of experimental temperatures and stresses considered. Test conditions of a transverse stress of 300 MPa and a temperature of 350 °C on MPTs capsules with varied crystallographic textures are sufficient to enable the dislocation creep to produce creep strains in the specimens tested.

5.2. Creep activation energy Q

Based on the creep tests on FS capsules at a temperature range from 300 °C to 400 °C under a transverse stress of 100, 150 and 200 MPa, the values of creep activation energy Q were obtained by plotting the slope of $\log \dot{\varepsilon}$ as a function of $1/T$ according to $Q = -R(\partial \log \dot{\varepsilon}/\partial(1/T))$ [5] as shown in Fig. 11, where R is the gas constant and T is the temperature.

The creep activation energies at transverse stresses of 100–200 MPa are ranging from 75.6 to 113.4 kJ/mol. There is insufficient data to distinguish better the three stress levels. The average value is 23.7 kcal/mol. It is known that thermal creep involves a thermally activated process, so, in principle, the value of Q should also indicate the creep mechanism operating in a given material under given conditions [5]. When dislocation-climb is the rate-controlled creep mechanism, creep activation energy is approximately equal to that of self-diffusion [5]. Holmes [33] reported that the determined creep activation energy from annealed and 20% cold-worked Zircaloy-2 at temperatures from 50 to 500 °C under stresses of 138–207 MPa is independent of stress, creep rate and temperature and is consistent with the reported self-diffusion activation energy. There are several reports about the activation energy for α-Zr self-diffusion, as listed in Table 6. As shown in Table 6, Shewfelt et al. [3,34] and Horvath et al. [35] reported the

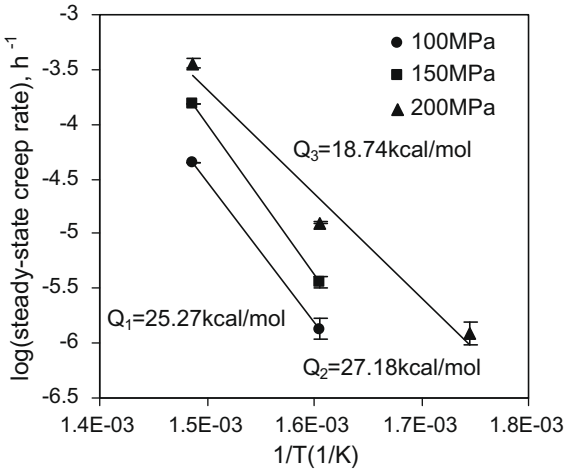

Fig. 11. Creep activation energy Q obtained by log–log relationship of steady-state creep rate in the transverse direction as a function of $1/T$ from FS capsules.

Table 6
Lists of activation energy of α-Zr self-diffusion from different references.

References	Activation energy of α-Zr self-diffusion
Shewfelt et al. [3,34]	302.4 kJ/mol at 450 °C
Horvath et al. [35]	337.68 kJ/mol at temperatures lower than 950 °C
Nakajima et al. [38]	67.2 kJ/mol at temperatures lower than 700 °C with impurity iron
King et al. [39]	
Davis et al. [40]	~126 kJ/mol for temperatures lower than 647 °C with impurity oxygen
Christodoulou et al. [31]	~88.2 and ~42 kJ/mol above and below 200 °C

Q value of α-Zr self-diffusion is about 302.4 kJ/mol and 337.68 kJ/mol, respectively. However, Hood [36,37] reported that the activation energy for self-diffusion of Zr is greatly reduced by extrinsic factors, especially the presence of iron and oxygen. He stated that the diffusion coefficient of iron in α-Zr is approximately eight orders of magnitude faster than the α-Zr self-diffusion coefficient over a range of temperatures [37]. It was proven that the average activation energy for diffusion of Fe in α-Zr is about 67.2 kJ/mol [38,39] and activation energy for oxygen diffusion to be about 126 kJ/mol for temperatures lower than 647 °C [40], Table 6. It was hypothesized by King et al. [39] that the self-diffusion of Zr at low temperatures reflects the behavior of an Fe-vacancy complex with a low activation energy. The values reported by Christodoulou et al. [31] in Table 6 were derived from the thermal creep tests on Zr–2.5Nb pressure tube materials. They attributed the low creep activation energy to the presence of iron. So, the current low value of Q could be the result of high extrinsic diffusivity paths provided by the impurity (e.g., Fe), which has a large binding energy with the dislocations and provides a high diffusivity paths acting as short circuit channels for the self-diffusion process [41].

With a stress exponent of ~3 and a creep activation energy Q, which is ~99.54 kJ/mol, dislocation creep is the likely deformation mechanism at 300–400 °C and 100–200 MPa, i.e., dislocation-climb is the rate-controlling mechanism and dislocation glide produces to the creep strains. This further supports our contention that dislocation glide is the strain-producing mechanism in the creep tests carried out at 300 MPa and 350 °C where the stress exponent is ~6.

5.3. Effect of grain size

From Fig. 8 and Table 4, it can be seen that the capsules of MPT63 exhibit substantially faster creep in both axial and transverse directions than those of MPT66 in spite of similar texture and grain morphology. Under a nominal transverse stress of 300 MPa at 350 °C, MPT66-05 crept over 1200 h to achieve 1% transverse strain; it took less than 400 h for MPT63-03. In Table 4, the steady-state creep rates of the MPT63 capsules are larger than those of the MPT66 capsules by a factor of four. The similar results were observed between the specimens from tubes MPT62 and 65, as shown in Fig. 9. This suggests an effect of grain size on creep of Zr–2.5Nb tubes. Although the grain size is not normally thought to affect creep behavior in most theories of dislocation creep, the sub-micron grain sizes of the MPT materials may represent a substantial grain boundary area to compete with dislocations as sinks and sources for vacancies and this may explain why tubes MPT63 and 62, with a finer grain structure, has a higher creep rate. Note that despite the different magnitudes of steady-state creep rate both have the similar creep anisotropy as evidenced by the steady-state creep rate ratios ($\dot{\varepsilon}_A/\dot{\varepsilon}_T$), consistent with their similar textures, as shown in Table 4. In power reactors, grain size also was reported to exhibit an influence on the

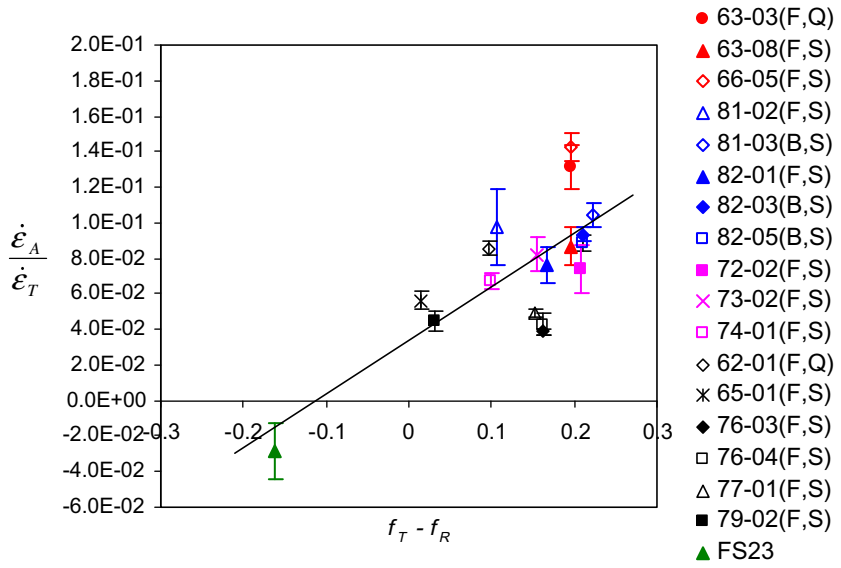

Fig. 12. Variation of steady-state creep rate ratios ($\dot{\varepsilon}_A/\dot{\varepsilon}_T$) as a function of texture parameters ($f_T - f_R$) for internally pressurized FS and MPT capsules under a nominal transverse stress of 300 MPa at 350 °C. (For interpretation of the references to colour in this figure legend, the reader is referred to the web version of this article.)

circumferential (transverse) creep strain of pressure tubes, i.e., the pressure tubes with a finer grain sizes exhibit higher transverse strain rates than those with a coarse grain size [4].

5.4. Creep anisotropy

The ratios of steady-state creep rate between the axial and transverse directions ($\dot{\varepsilon}_A/\dot{\varepsilon}_T$) is a measure of the creep anisotropy of internally pressurized Zr alloys tubes ($\dot{\varepsilon}_A/\dot{\varepsilon}_T$) in which the basal plane normals are predominantly distributed in the radial/transverse plane [11]. Fig. 12 shows the variation of ($\dot{\varepsilon}_A/\dot{\varepsilon}_T$) as a function of the texture parameter ($f_T - f_R$) for all the internally pressurized FS and MPT capsules tested under a nominal transverse stress of 300 MPa at 350 °C. There is an obvious creep anisotropy dependence on the crystallographic textures of the tubes. With increasing ($f_T - f_R$), the steady-state creep ratio ($\dot{\varepsilon}_A/\dot{\varepsilon}_T$) increases. In general, the tubes (MPT63 and 66) with an extrusion ratio of 10:1 at 815 °C have the highest values of ($\dot{\varepsilon}_A/\dot{\varepsilon}_T$), followed by tubes MPT81 and 82 with an extrusion ratio of 10:1 at 975 °C, tubes MPT72, 73 and 74 with an extrusion ratio of 10:1 at 650 °C, and tubes MPT76, 77, 79, 62 and 65 with an extrusion ratio of 4:1 at 650 °C in a decreasing order. The FS tube exhibits a negative ($\dot{\varepsilon}_A/\dot{\varepsilon}_T$) value corresponding to $f_R > f_T$, indicating the poorest creep resistance in the transverse direction in the tested tubes. For each group of tubes with the same nominal extrusion conditions (marked as the same color and symbol in Fig. 12), the steady-state creep rate ratios ($\dot{\varepsilon}_A/\dot{\varepsilon}_T$) fall into a similar range.

Grain size does not appear to be a factor significantly affecting the creep anisotropy, e.g., the values of steady-state creep rate ratios for MPT63-03 (a fine grain size) and MPT66-05 (a coarse grain size) are similar, although a finer grain size leads to a faster creep, as shown in Figs. 8 and 9. Moreover, the grain structure differences within the tubes with the same nominal extrusion conditions seem not to influence the creep anisotropy, e.g., the values of ($\dot{\varepsilon}_A/\dot{\varepsilon}_T$) for the front and back ends capsules of tubes MPT81 and 82, are in a similar range ($7.6–10.4 \times 10^{-2}$) and are close to the linear trend line representing the overall effect of texture in Fig. 12. MPT62-01(F,Q) (equiaxed grain shape in radial–transverse section) shows the highest value of steady-state creep rate ratios in the group with an extrusion ratio of 4:1 at 650 °C, but its value of ($\dot{\varepsilon}_A/\dot{\varepsilon}_T$) is located at a similar distance above the trend line as that of MPT65-01(F,S) (elongated grain shape) in spite of different grain structures. Furthermore, the distribution of β-phase also has no apparent effect on the creep anisotropy, e.g., tube MPT62 and the back ends of tubes MPT81 and 82 have the β-phase broken up into discrete particles as opposed to the more continuous distribution of the other tubes, but their ($\dot{\varepsilon}_A/\dot{\varepsilon}_T$) values are all in a similar range among the tubes with the same extrusion conditions. In brief, the only microstructural factor of *those examined* which obviously correlates with creep anisotropy is crystallographic texture. Although there may be small effects of grain structure, size and β-phase distribution on the creep anisotropy of the cold-worked Zr–2.5Nb tubes, these are within the experimental error.

The anisotropic hcp structure and strong texture of the materials are clearly key factors determining the creep anisotropy. Since the likely deformation mechanism is dislocation creep, the anisotropy of slip in the hcp Zr crystal, likely determines this anisotropy. At room temperature, in polycrystalline Zr–2.5Nb, the critical resolved shear stresses for $1/3\langle 11\bar{2}0\rangle, \{1\bar{1}00\}$, $1/3\langle 11\bar{2}0\rangle, (0002)$ and $1/3\langle 11\bar{2}3\rangle, \{1\bar{1}01\}$ slip are in the approximate ratios of 1:1.25:2.25/3.42[3] by Cai et al. [42]. At high temperatures (>600 °C) in pure Zr single crystals under compression they are in the approximate ratios of 1:2.6:13 [43]. Crystals deforming by slip are, hence, substantially stronger along the *c*-axis than in the basal plane, a situation that leads qualitatively to the variation in ($\dot{\varepsilon}_A/\dot{\varepsilon}_T$) versus ($f_T - f_R$) seen in Fig. 12 [11].

Another factor that could affect the anisotropy from slip is the distribution of different dislocation types from cold work amongst the different grain orientations, as seen by Griffiths et al. [2]. Typically cold-worked Zr–2.5Nb tubes have dislocation densities $\sim 3 \times 10^{14}$ and $5 \times 10^{13}\ m^{-2}$ [4,44] (dislocations with a Burgers vector of $1/3\langle 11\bar{2}0\rangle$ and $1/3\langle 11\bar{2}3\rangle$, respectively) after stress relieving for 24 h at 400 °C, so these are likely to be persistent during creep testing at 350 °C. The distribution of different dislocation

[3] Cai [42] found the critical resolved shear stress for pyramidal slip to be higher for compression normal to the slip plane than for tension normal to the slip plane.

types amongst different crystal orientations thus may be another factor affecting the creep anisotropy.

6. Conclusions

Biaxial creep tests ($\sigma_A/\sigma_T = 0.48$) were carried out on cold-worked Zr–2.5Nb tubes with a variety of crystallographic textures and microstructures.

A stress exponent for creep, n, was obtained which varies from about 3 to 3.9–7.3 as a transverse stress increases from 100 to 325 MPa with a transition at about 250 MPa. An average stress exponent of 6.4 is obtained from the tests under a transverse stress of 250–325 MPa at 350 °C. An average value of 99.54 kJ/mol was determined for creep activation energy at lower stresses. These values of stress exponents and creep activation energy establish a regime in which dislocation slip is the likely strain-producing mechanism.

Creep tests were performed on MPT and FS capsules with varied crystallographic textures and microstructures under a transverse stress of 300 MPa at 350 °C. It was showed that the steady-state creep rate ratio, $(\dot{\varepsilon}_A/\dot{\varepsilon}_T)$ exhibited an approximately linear increasing trend as the resolved faction of basal plane normals $(f_T - f_R)$ increases. Finer grain size resulted in faster creep behaviors. The values of $(\dot{\varepsilon}_A/\dot{\varepsilon}_T)$ are consistent in the tubes with the same textures but the different grain sizes. Although there may be small effects of grain structure and β-phase distribution on the creep anisotropy of the cold-worked Zr–2.5Nb tubes, these are within the experimental error. The only microstructural factor of *those examined* which obviously correlates with creep anisotropy $(\dot{\varepsilon}_A/\dot{\varepsilon}_T)$ is crystallographic texture.

Acknowledgements

The authors would like to thank Nu-Tech Precision Metals Inc. for manufacturing the micro pressure tubes, R. Rogge and M. Gharghouri of the National Research Council of Canada for help with texture measurements, F. Butcher of Atomic Energy of Canada Ltd. for pressurization of the creep capsules, Y. Zhang, I. Yakubtsov and A. Khan of Queen's University for programming the Z-Mike laser sensor system and for assistance with TEM. This research is sponsored by Natural sciences and Engineering Research Council of Canada, the CANDU Owners Group Inc., Ontario Power Generation Inc. and Nu-Tech Precision Metals Inc. under the Industrial Research Chair Program in Nuclear Materials at Queen's University.

References

[1] Atomic Energy of Canada Limited, Canada Enters the Nuclear Age: A Technical History of Atomic Energy of Canada Limited, McGill-Queen's University Press, 1997.
[2] M. Griffiths, R.A. Holt, J. Li, S. Saimoto, Microstructure Science, vol. 26, ASM International, Berlin, 1998. pp. 293–301.
[3] R.S.W. Shewfelt, L.W. Lyall, D.D. Godin, J. Nucl. Mater. 125 (1984) 228–235.
[4] M. Griffiths, W.G. Davies, G.D. Moan, A.R. Causey, R.A. Holt, S.A. Aldridge, ASTM-STP 1423 (2002) 796–808.
[5] D.G. Franklin, G.E. Lucas, A.L. Bement, ASTM-STP 815 (1983).
[6] A.R. Causey, V. Fidleris, S.R. MacEwen, C.W. Schulte, ASTM-STP 956 (1987) 54–68.
[7] R.G. Fleck, J.E. Elder, A.R. Causey, R.A. Holt, ASTM-STP 1245 (1994) 168–182.
[8] A.R. Causey, R.A. Holt, N. Christodoulou, E.T.C. Ho, ASTM-STP 1354 (2000) 74–85.
[9] R.A. Holt, J. Nucl. Mater. 372 (2008) 182–214.
[10] R. Levi, M.P. Puls, in: Proc. 18th Int. Conf. on Structural Mechanics in Reactor Technology (SMiRT 18), Beijing Paper G10-3, 2005.
[11] N. Christodoulou, A.R. Causey, C.H. Woo, C.N. Tomé, R.J. Klassen, R.A. Holt, ASTM-STP 1175 (1994) 1111–1128.
[12] A.R. Causey, J.E. Edler, R.A. Holt, R.G. Fleck, ASTM-STP 1245 (1994) 202–220.
[13] R.A. Holt, S.A. Aldridge, J. Nucl. Mater. 135 (1985) 246–259.
[14] H.G. Kim, Y.H. Kim, B.K. Choi, Y.H. Jeong, J. Nucl. Mater. 359 (2006) 268–273.
[15] R. Choubey, J.A. Jackman, Metal. Mater. Trans. A 27A (1996) 431–440.
[16] A. Perovic, V. Perovic, G.C. Weatherly, G.R. Purdy, R.G. Fleck, J. Nucl. Mater. 199 (1993) 102–111.
[17] M. Griffiths, W. Phythian, S. Dumbill, J. Nucl. Mater. 207 (1993) 353–356.
[18] G.M. Hood, J. Nucl. Mater. 159 (1988) 149–175.
[19] G.M. Hood, H. Zou, D. Gupta, R.J. Schultz, J. Nucl. Mater. 223 (1995) 122–125.
[20] H.E. Rosinger, J. Bowden, R.S.W. Shewfelt, AECL 6647 (April) (1982).
[21] Y. Li, R. Rogge, R.A. Holt, Mater. Sci. Eng. A 437 (2006) 10–20.
[22] R.A. Holt, P. Zhao, J. Nucl. Mater. 335 (2004) 520–528.
[23] P. Zhao, R.A. Holt, Mater. Sci. Forum 475–479 (2005) 1421–1424.
[24] H.M. Chung, R.S. Daum, J.M. Hiller, M.C. Billone, ASTM-STP 1432 (2002) 561–582.
[25] R.A. Holt, E.F. Ibrahim, Acta Metal. 27 (1979) 1319–1328.
[26] C. Judge, Unpublished Data, Queen's University.
[27] M.E. Kassner, M.-T. Pérez-Prado, Proc. Mater. Sci. 45 (2000) 1–102.
[28] H.J. Frost, M.F. Ashby, Deformation–Mechanism Maps, Pergamon Press, Oxford, 1982.
[29] E. Kohn, ASTM-STP 633 (1977) 402–417.
[30] K. Nuttall, Scripta Metal. 10 (1976) 835–840.
[31] N. Christodoulou, P.A. Turner, C.N. Tomé, C.K. Chow, R.J. Klassen, Metal. Mater. Trans. A 33 (2002) 1103–1115.
[32] T.A. Hayes, M.E. Kassner, Metal. Mater. Trans. A 37 (2006) 2389–2396.
[33] J.J. Holmes, J. Nucl. Mater. 13 (1964) 137–141.
[34] R.S.W. Shewfelt, Can. Metal. Q. 23 (1984) 441–445.
[35] J. Horvath, F. Dyment, H. Mehrer, J. Nucl. Mater. 126 (1984) 206–214.
[36] G.M. Hood, Defect Diffus. Forum 95–98 (1993) 755–774.
[37] G.M. Hood, J. Nucl. Mater. 135 (1985) 292–295.
[38] H. Nakajima, G.M. Hood, R.J. Schultz, Phil. Mag. B 58 (1988) 319–337.
[39] A.D. King, G.M. Hood, R.A. Holt, J. Nucl. Mater. 185 (1991) 174–181.
[40] M. Davis, K.R. Montgomery, J. Standring, J. Inst. Metals 89 (1961) 172–174.
[41] A.M. Garde, J. Nucl. Mater. 80 (1979) 195–206.
[42] S. Cai, M.R. Daymond, R.A. Holt, Acta Mater. 47 (2009) 409–417.
[43] A. Akhtar, J. Nucl. Mater. 47 (1973) 79–86.
[44] R.A. Holt, J. Nucl. Mater. 59 (1976) 234–242.